

Free water DTI estimates from single b-value data might seem plausible but must be interpreted with care

Marc Golub¹, Rafael Neto Henriques^{2 †}, Rita G. Nunes^{1 †}

¹Institute for Systems and Robotics and Department of Bioengineering, Instituto Superior Técnico, Universidade de Lisboa, Lisbon, Portugal

²Champalimaud Research, Champalimaud Centre for the Unknown, Lisbon, Portugal

†These authors contributed equally to this work.

Corresponding Author: Rita G. Nunes

Institute for Systems and Robotics,

Instituto Superior Técnico,

Av. Rovisco Pais, 1

1049-001 Lisboa, Portugal

Phone: +351.218418277

Fax: +351.218418291

E-mail: ritagnunes@tecnico.ulisboa.pt

Abstract

Purpose

Free water elimination diffusion tensor imaging (FWE-DTI) has been widely used to distinguish increases of free water (FW) partial volume effects from tissue's diffusion in healthy ageing and degenerative diseases. Since the FWE-DTI fitting is only well posed for multi-shell acquisitions, a regularized gradient descent (RGD) method was proposed to enable application to single-shell data, more common in the clinic. However, the validity of the RGD method has been poorly assessed. This study aims to quantify the specificity of FWE-DTI procedures on single- and multi-shell data.

Methods

Different FWE-DTI fitting procedures were tested on an open-source in vivo diffusion dataset and single- and multi-shell synthetic signals, including the RGD and standard non-linear least squares (NLS) methods. Single-voxel simulations were carried out to compare initialization approaches. A multi-voxel phantom simulation was performed to evaluate the impact of spatial regularization when comparing between methods. To test the algorithms' specificity, phantoms with two different types of lesions were simulated: with increased mean diffusivity (MD) or with increased FW.

Results

Plausible parameter maps were obtained with RGD from single-shell in vivo data. The plausibility of these maps was shown to be determined by the initialization. Tests with simulated lesions inserted into the in vivo data revealed that the RGD approach cannot distinguish FW from tissue MD alterations, contrarily to the NLS algorithm.

Conclusion

RGD FWE-DTI has limited specificity and, thus, its results from single-shell data should be carefully interpreted. When possible, multi-shell acquisitions and the NLS approach should be preferred instead.

Keywords: free-water elimination DTI, single-shell data, regularized gradient descent, non-linear least squares FWE-DTI.

1 Introduction

Diffusion-weighted Magnetic Resonance Imaging (dwMRI) is a non-invasive imaging modality sensitive to microscopic tissue properties beyond the macroscopic spatial resolution offered by current MRI scanners (1). The information captured by dwMRI is multi-dimensional and its sensitivity to different diffusion properties depends on the acquisition parameters. For example, diffusion tensor imaging (DTI) can estimate diffusion anisotropy from dwMRI images acquired with different gradient directions for a single level of diffusion-weighting (i.e. single-shell acquisition) (2). Another technique, diffusion kurtosis imaging, allows estimating non-Gaussian diffusion properties from dwMRI images acquired with different contrast levels (i.e. multi-shell acquisition) (3,4). Although both are sensitive to tissue alterations undetected by conventional structural images (1,5), the derived metrics are not specific to concrete microstructural properties and are thus hard to interpret (6–8).

To improve dwMRI's specificity, microstructural models have been introduced to directly extract biophysical measures (6,9–11). However, assumptions and constraints are often required to minimize the number of parameters to be estimated (8,12). For instance, several studies used a simplified tissue model, with two compartments assigned to intra- and extra-cellular media to estimate axonal water fraction and diameter (13–17). Two-compartmental models have also been used to decouple free water (FW) contributions from the tissue's diffusion tensor in FW elimination DTI (FWE-DTI) (18,19).

FWE-DTI has attracted a huge interest to characterize diffusion alterations in the context of healthy aging (20,21) and neurodegeneration associated with Alzheimer's Disease (22), Parkinson's Disease (23), and Traumatic Brain injury (24). These studies suggest that FWE-DTI is fundamental to decouple changes associated with microstructural alterations from increases in partial volume near interfaces between tissue and cerebrospinal fluid (CSF); in particular, partial volume increases associated with gross tissue atrophy and ventricular enlargement. Moreover, compared to suppression techniques based on fluid attenuated inversion recovery (FLAIR) (25,26), FWE-DTI has the advantage of providing a FW fraction estimate, a potential surrogate marker for edema (19,27).

As any other two-compartmental model, FWE-DTI is only well-posed for multi-shell acquisitions (28,29). Previous studies successfully showed that the apparent FW fraction can be estimated from such acquisitions by combining linear and non-linear approaches (25,29,30). However, since single-shell acquisitions are clinically more prevalent due to time constraints, several single-shell FWE-DTI procedures have been proposed based on spatially regularized gradient descent (RGD) algorithms, requiring careful initialization (19,27,31). Although single-shell FWE-DTI procedures were shown to provide plausible FW maps, their use in clinical applications remains controversial - these algorithms have been poorly validated (plausibility does not imply specificity) and no clear theoretical explanation has been provided on how they recover information on the bi-exponential nature of the FWE-DTI model. Moreover, no single-shell FWE-DTI procedure is currently available in an open-source software, hampering independent and objective validation and comparison with other FW estimation techniques.

In this study, state-of-the-art FWE-DTI fitting procedures RGD algorithms are revisited. Our main objective was to quantify the specificity of FWE-DTI estimates when extracted from single- and multi-shell dwMRI acquisitions. The plausibility of FWE-DTI estimates is first illustrated on openly available dwMRI data. Based on numerical simulations, we investigated which FWE-DTI fitting procedures steps determine the plausible contrast of obtained FW maps. At last, the specificity of FW maps from single- and multi-shell acquisitions was quantitatively assessed on synthetic phantoms to which different lesions were introduced. For reproducibility, all tested FWE-DTI fitting procedures were incorporated into the open-source library diffusion in python (DIPY) (32).

2 Theory

2.1 FWE-DTI model

In FWE-DTI, a two-compartmental model is used to account for FW contamination (18,19). Assuming that the repetition time (TR) is sufficiently long to ignore T1 relaxation, this model can be described by:

$$S_k(D_t, \nu, \rho_t, \rho_w, T2_t, T2_w) = \nu \rho_t \exp\left(-\frac{TE}{T2_t}\right) \exp(-b_k n_k^T D_t n_k) + (1 - \nu) \rho_w \exp\left(-\frac{TE}{T2_w}\right) \exp(-b_k D_w),$$

[1]

where ν is the volumetric tissue fraction, ρ_t and ρ_w are the tissue and water proton densities, $T2_t$ and $T2_w$ are the tissue and FW transverse relaxation times, TE is the acquisition echo time, D_t is the tissue's apparent diffusion tensor (with 6 independent elements (2)), $D_w = 3 \mu m^2 ms^{-1}$ is the constant diffusivity of isotropic FW at body temperature ($\cong 37^\circ$) (33), b_k is the diffusion weighting for the k^{th} acquisition and n_k the respective gradient direction (normalized column vector; T denotes the transpose). This model assumes no water exchange between the two compartments and that both display Gaussian diffusion (19).

Since decoupling the volumetric tissue fraction ν from parameters ρ_t , ρ_w , $T2_t$, and $T2_w$ would require additional relaxometry measurements, the effective tissue water fraction is often defined as $f = \nu S_t / S_0$, where S_0 is the signal measured at b-value $b_0 = 0$ (i.e. $S_0 = \nu S_t + (1 - \nu) S_w$), S_t is the reference b_0 signal from voxels containing only grey matter (GM) and white matter (WM) tissues (assuming all tissue presents a single $T2_t$ value, $S_t = \rho_t \exp(-TE/T2_t)$), and S_w is the reference b_0 signal from voxels containing only FW ($S_w = \rho_w \exp(-TE/T2_w)$). Inserting the effective tissue water fraction f into Eq. 1, the FWE-DTI model can be rewritten as:

$$A_k(D_t, f) = f \exp(-b_k n_k^T D_t n_k) + (1 - f) \exp(-b_k D_w),$$

[2]

where A_k is the diffusion signal attenuation (i.e., $A_k = S_k / S_0$). From Eq. 2, the effective FW fraction is defined as $f_w = 1 - f$. Note that if ρ_t , ρ_w , $T2_t$, and $T2_w$ are known, the effective fractions can be converted to actual volumetric fractions $\nu = f S_w / (S_t + f(S_w - S_t))$.

Despite its simplicity, Eq. 2 is a two-compartmental model and has thus a flat fitting solution landscape, i.e. similar residuals are observed for different D_t samples for any given $f \in [0,1]$ as shown in (28) so that choosing the most viable pair (Dt, f) is not straightforward.

2.2 Regularized Gradient Descent fitting procedure

To fit the FWE-DTI model to single-shell data, previous studies proposed using regularized gradient descent (RGD) algorithms with careful parameter initializations (19,27,31,34). The different initialization procedures and the RGD algorithm implemented and tested in this study are

described in the next subsections. Notably, although these procedures were designed for single-shell acquisitions, all these can also be adapted to multi-shell datasets (vide infra).

2.2.1 Parameter initialization

Three different strategies were tested to initialize f in the RGD algorithm.

Initialization based on the T2-weighted images: this empirical estimation (here referred to as f_{S_0}) assumes that regions with higher FW fraction present hyperintense T2-weighted signals (S_0) (19):

$$f_{S_0} = 1 - \log(S_0/S_t^r)/\log(S_w^r/S_t^r), \quad [3]$$

where S_t^r and S_w^r are, respectively, the reference signal intensities for voxels containing either tissue or free diffusing water only, and can be estimated from regions of interest placed on deep WM or the ventricles (19). To avoid implausible estimates, f_{S_0} values are constrained:

$$\frac{\min(\hat{A}_k - \exp(-b_k D_w))}{\max(\exp(-b_k \lambda_{\min}) - \exp(-b_k D_w))} \leq f_{S_0} \leq \frac{\max(\hat{A}_k - \exp(-b_k D_w))}{\min(\exp(-b_k \lambda_{\max}) - \exp(-b_k D_w))}, \quad [4]$$

where \hat{A}_k is the measured signal decay, λ_{\min} and λ_{\max} are the minimum and maximum expected tissue diffusivities (0.1 and $2.5 \mu m^2 ms^{-1}$, respectively (19)). The equation was modified for compatibility with multi-shell data, and to correct for the swapped denominators in (19).

Initialization based on a tissue's Mean Diffusivity prior: to avoid relying on the non-quantitative S_0 images, tissue water estimates (here referred to as f_{MD}) can be initialized based on a fixed prior for the tissue's Mean Diffusivity (MD) (31):

$$f_{MD} = \frac{\exp(-b MD) - \exp(-b D_w)}{\exp(-b MD_t^{ref}) - \exp(-b D_w)}, \quad [5]$$

where MD is computed with standard DTI, MD_t^{ref} is the fixed tissue's MD prior (set to $0.6 \mu m^2 ms^{-1}$ (31,34)), and b the single shell b-value. For multiple-shell acquisitions, one b-value is

empirically selected ($1 \text{ ms } \mu\text{m}^{-2}$ in our study) which provides sufficient diffusion contrast while minimizing non-Gaussian diffusion effects not considered by FWE-DTI (19). Notably, voxels with higher MD values will present higher f_{MD} . Unlike f_{S0} , f_{MD} is constrained by 0 and 1.

Hybrid initialization (f_{hybrid}): to combine T2-weighted and dwMRI information, a log-linear interpolation can be performed between f_{S0} and f_{MD} estimates (31,34):

$$f_{hybrid} = f_{S0}^{1-\alpha} \times f_{MD}^{\alpha}, \quad [6]$$

where α determines their relative weights. To assign a higher weight to f_{MD} in regions with T2-weighted signals closer to typical tissue intensities (i.e. healthy tissue) and higher weights to f_{S0} in hyperintense voxels (i.e. edematous tissue), α is set to the initial tissue water fraction computed by Eq. 3 but unconstrained by f_{min} and f_{max} (Eq. 4) (34).

Initialization of tissue's diffusion tensor: The tissue fraction initializations were used to estimate the normalized tissue's signal attenuation $[A_t]_k = (\hat{A}_k - (1 - f) \exp(-b_k D_w)) / f$. For each initialization (f_{S0} , f_{MD} , and f_{hybrid}), an initial estimate of D_t was obtained by fitting the standard DTI model to $[A_t]_k$.

2.2.2 Regularized Gradient Descent

Here, we implemented an adapted version of the FWE-DTI fitting framework that constrains D_t to be spatially smooth by introducing a regularization term into the minimization functional (19):

$$L(D_t, f) = \int_{\Omega} \left[\sum_{k=1}^2 (A_k(D_t, f) - \hat{A}_k)^2 + \omega \sqrt{|\gamma(D_t)|} \right] d\Omega, \quad [7]$$

where Ω represents the image domain, $A_k(D_t, f)$ is the predicted signal attenuation given by Eq. 2, \hat{A}_k is the measured signal attenuation for the k^{th} gradient direction, $|\gamma(D_t)|$ is the determinant of the induced metric which acts as a regularizer, and ω a hyperparameter for controlling its weight (19). The metric tensor is computed from the spatial derivatives of D_t and was chosen to be Euclidean to reduce computational burden (27). These concepts are borrowed from the field of

differential geometry; application to diffusion tensors is further explained in (19,35); the Euclidean metric implementation is described in (27).

Minimization of Eq. 7 can be done with a gradient descent scheme, following the iteration rules provided in (19,27). Here, a small correction is proposed to the fidelity term ΔF_i in (19), obtained by differentiating the first term of Eq. 7 with respect to each independent diffusion component X^i (i ranges from 1 to 6):

$$\Delta F^i = \sum_{k=1} (A_k(D_t, f) - \hat{A}_k) f \exp(-b_k n_k^T D_t n_k) \left(b_k n_k^T \frac{\partial D_t}{\partial X^i} n_k \right), \quad [8]$$

where $\frac{\partial D_t}{\partial X^i}$ is the partial derivative of D_t with respect to X^i . Minimization of the second term in Eq. 7 gives rise to the Laplace-Beltrami operator (19,27).

Differentiating Eq. 7 with respect to f gives the tissue fraction increment, again slightly different from that presented in (19):

$$\Delta f = \sum_{k=1} (A_k(D_t, f) - \hat{A}_k) (f \exp(-b_k n_k^T D_t n_k) - \exp(-b_k D_w)). \quad [9]$$

2.2.3 Dealing with voxels containing only free water

FWE-DTI estimates are not well defined for voxels containing only FW (25,29). Since their signal is well-described by a single exponential with high isotropic diffusion (i.e. $\sim 3 \mu m^2 ms^{-1}$), D_t can erroneously be fitted with a diffusion tensor with a large trace and FW assigned any value between 0 and 1. To ensure a FW estimate close to 1, initial parameter estimates with high tissue MD can be re-adjusted to have $f = 0$ and D_t assigned null elements. Tissue MD is classified as high if above $1.5 \mu m^2 ms^{-1}$ (25,29). To avoid low precision FWE-DTI estimates in regions with low tissue contributions, refined tissue MD and fractional anisotropy (FA) estimates are set to zero when the refined f is below 0.1 (25,29).

2.3 Standard least squares fitting procedure

The FWE-DTI model has a unique (D_t, f) solution when multi-shell data is available, providing a reference for regularized single-shell fitting procedures. Here a 2-step minimization based on a combination of standard weighted linear least squares (WLS) and non-linear least square (NLS) routines was used as reference multi-shell FWE-DTI fitting procedure (25,29).

3 Methods

3.1 MRI Data

A dwMRI dataset of a healthy volunteer acquired in a Siemens Prisma 3T scanner was used (<https://digital.lib.washington.edu/researchworks/handle/1773/33311>), including b-values 0.2, 0.4 $ms \mu m^{-2}$ (8 directions per shell, sampled twice) and 1, 2, 3 $ms \mu m^{-2}$ (90 directions per shell); an unweighted image was acquired every 8th or 9th volume. Other relevant imaging parameters: isotropic resolution of 2 mm, multi-band factor of 3, $TR = 3000 ms$, $TE = 74 ms$ and flip angle of 72 °. This dataset had been previously pre-processed to correct for eddy currents distortions and motion using FSL tools (36,37) and incorporated into DIPY. In addition, here this dataset is corrected for B1 field inhomogeneities using “dwibiascorrect” from MRTrix3 with the FSL-FAST option (38).

This data was used to provide a qualitative assessment of the different FWE-DTI estimates before our quantitative analysis. For this, all dwMRI images acquired with b-values larger than 1 $ms \mu m^{-2}$ were removed to avoid non-Gaussian diffusion effects (25,29). Diffusion parameter maps were extracted and compared between: 1) standard DTI model (using DIPY’s WLLS fitting (32)); 2) FWE-DTI model using the regularized gradient descent algorithm including only the data with $b = 0$ and 1 $ms \mu m^2$ (RGD, single-shell); 3) FWE-DTI model using the regularized gradient descent algorithm on all b-values $\leq 1 ms \mu m^2$ data (RGD, multi-shell); 4) FWE-DTI model using the standard non-linear approach (25,29) (NLS, multi-shell). For simplicity, the single- and multi-shell RGD algorithm for this first assessment was initialized with the hybrid initialization technique (34).

3.2 Simulations

Quantitative analyses to assess the robustness of different FWE-DTI fitting steps were first performed based on single- and multi-voxel synthetic phantoms. For this purpose, dwMRI signals were numerically generated using Eq.1 with: ρ_t and ρ_w set to typical proton density values (70% and 100% (39)); TE set to 74 ms (as for the in vivo dataset); $T2_t$ and $T2_w$ set to 80 ms and 500 ms, typical 3T transverse relaxation times for tissue (40) and CSF (41). Ground truth tensors were simulated considering reference values for the D_t 's eigenvalues: $\lambda_1^{WM} = 1.6$, $\lambda_2^{WM} = 1.5$ and $\lambda_3^{WM} = 0.3 \mu m^2 ms^{-1}$ (typical for WM (29)), corresponding to $FA_t^{WM} = 0.7$ and $MD_t^{WM} = 0.8 \mu m^2 ms^{-1}$. Synthetic signals were simulated using the forward model (Eq. 1) and Rician noise was added to achieve a signal-to-noise ratio (SNR) of 40 (reference S_0 SNR for FW voxels).

Single-voxel simulations: to compare between initialization methods, single-voxel simulations were repeated for D_t with different MD_t ground truth values (sampled between 0.1 and $1.6 \mu m^2 ms^{-1}$). To maintain FA_t^{WM} , the eigenvalues of D_t were computed by $\lambda_1^{gt} = c\lambda_1^{WM}$, $\lambda_2^{gt} = c\lambda_2^{WM}$, and $\lambda_3^{gt} = c\lambda_3^{WM}$, where $c = MD_t/MD_t^{WM}$. Simulations were also repeated for different tissue water fraction values f linearly spaced between 0 and 1, converted to volume fractions v to generate the synthetic dwMRI signals using Eq.1. For each ground truth (f, MD_t) pair, 100 different directions were considered for the principal orientation of D_t and for each orientation, single-shell signals were generated along 32 gradient directions with $b = 1 \mu m^2 ms^{-1}$. and six S_0 images. Synthetic Rician noise was added for 100 noise instances and the initialization methods were applied to each single-voxel signal. The median and inter-quartile ranges of the f , FA_t and MD_t estimates were computed over the 100 repeated D_t directions times 100 noise instances.

Multi-voxel phantom: this phantom was designed to assess if applying spatial regularization to the RGD algorithm improves the estimates of FWE-DTI in a best-case scenario (i.e. phantom with a smooth D_t field). For this purpose, a multi-voxel phantom ($21 \times 21 \times 21$ voxels) of a cylindrical fiber (radius of 7 voxels) was designed, with flat ground truth D_t . The fiber was contaminated with three levels of effective FW fraction $f_w = 0.1, 0.4$ and 0.7 that increased along the radial direction while kept constant along the axial direction. To compare the FWE-DTI with DIPY's multi-shell fitting procedure (NLS FWE-DTI (25)), besides the single-shell scenario, simulations considered a multi-shell dataset with b-values of 0.5 and $1 ms \mu m^2$ (32 directions per shell), with six S_0 images. Standard DTI and the RGD procedure for the FWE-DTI model were applied to both data (RGD single- and multi-shell for short), while the NLS FWE-DTI was applied

to the multi-shell data only. The estimated f_w , FA_t and MD_t maps were visually assessed, and the medians of the initial and final FWE-DTI parameter estimates compared to the ground truth values.

In-vivo data with simulated lesions: the aim was to evaluate the specificity of FWE-DTI parameter estimates, i.e. whether these enable decoupling alterations to D_t from changes in the degree of FW contamination. For this, two types of synthetic lesions were inserted into a representative dwMRI brain dataset: 1) lesions with increased FW content (FW lesion); and 2) lesions with increased MD_t (MD lesion). Ground truth FWE-DTI parameter maps were obtained by applying the gold standard NLS FWE-DTI technique (25). Lesions covering a spherical volume (radius of 14 mm) were placed in a WM region near the superior portion of the left internal capsule. The lesions were generated by increasing the f_w ground truth values to 0.6 (FW lesion) or by increasing MD_t to $1.1 \mu m^2 ms^{-1}$ without changing the ground truth FA_t (as described for the single-voxel simulation). The GT parameters were plugged into (Eq.1) to generate, for each lesion type, single- and multi-shell data with the same number of directions and b-values as described for the multi-voxel phantom. All non-diffusion parameters of the lesions were as for the synthetic phantoms. Standard DTI and RGD FWE-DTI (for the best performing initialization technique according to the phantom simulations) were applied to all single- and multi-shell datasets, while the NLS algorithm was applied only to the multi-shell data. The multi-shell data were also processed with a modified NLS algorithm, using the best performing single-shell initialization for a fairer comparison (same initialization). The estimated scalar maps were compared with the ground truth parameters to assess specificity.

For every run of the RGD routine, unless stated otherwise, the number of iterations was 200, the learning rate was 0.0005, and the spatial regularization operator was turned off halfway (ω was set to 0 at iteration 100) according to (19). To promote the reproducibility of our results, the code used for all simulations are available on an open source repository (<https://github.com/mvgolub/FW-DTI-Beltrami>).

4 Results

Figure 1 shows the estimated scalars maps from a healthy human brain. The f_w maps show values near one for all FWE-DTI fitting procedures in regions comprising the brain ventricles and surrounding the parenchyma (first row). The corresponding MD_t values were always lower than obtained using standard DTI (second row). Both RGD single- and multi-shell procedures provided

MD_t maps with lower grey to WM contrast compared to NLS FWE-DTI. The FA maps look similar for all methods (third row), but the FWE-DTI estimates were higher than the DTI estimate, particularly for WM regions.

The results obtained for the single-voxel simulations are presented in Figure 2. For the case of fixed ground truth $MD_t = 0.6 \mu m^2 ms^{-1}$ and varying f_w (first column), the initialization based on MD_t (blue markers) shows the smallest deviations to the ground truth line (in orange). When f_w was fixed at 0.2, 0.5 or 0.8 and MD_t deviated from $0.6 \mu m^2 ms^{-1}$ (second, third and fourth columns), the MD_t and hybrid (green) initializations differs more from the ground truth values. The performance of the S_0 based initialization (red markers) was invariant to the ground truth MD_t (second, third and fourth columns), but the FWE-DTI estimates present a constant bias.

Scalar maps estimated for the single-shell dataset of the synthetic multi-voxel phantom are presented on the left side of Figure 3. Although no spatial variation was simulated on MD_t and FA ground truth maps (first column), f_w contamination induced a spatial variation on the standard DTI FA and MD maps (second column). FA, and MD_t initial estimates obtained using the hybrid method (third column) show a lower spatial dependence compared to DTI estimates. The fourth column shows the FWE-DTI estimates refined using the RGD single-shell algorithm, showing identical contrast to the initial estimates. The median and interquartile ranges of the FWE-DTI parameter errors computed before ('init') and after ('est') applying the RGD algorithm are shown on the right side of Figure 3 for all initialization methods (left to right: S_0 , MD_t and hybrid methods). The latter plots confirm that refined estimates present similar accuracy and precision to their initial estimates, with the hybrid initialization resulting in smaller bias levels.

Figure 4 shows the analogous results for the multi-shell dataset of the multi-voxel phantom. Both hybrid initialization and RGD estimates present higher precision (lower interquartile ranges) than the NLS estimates, but they show lower estimate precision (higher deviation between estimates median and ground truth values). The interquartile range for the refined RGD estimates ('est') are slightly lower than the initial estimates ('ini') (right side of Figure 4).

The results for the synthetic lesions are presented in Figures 5 and 6 for FW and MD lesions, respectively. All FWE-DTI fitting routines were able to estimate the high f_w increases in the FW lesion area (true positives pointed by the cyan arrows). Both the standard DTI, and single-shell RGD erroneously estimated an increased MD (false positives pointed by red arrow) in the FW lesion. Moreover, this FWE-DTI technique removed the MD_t contrast between GM and WM regions. For MD lesions (Figure 6), the single- and multi-shell RGD algorithms (third and fourth

columns) erroneously estimated increased f_w values in the lesion (false positives pointed by the red arrow). The slight increase in MD (second row) is, however, still captured by the RGD particularly for the multi-shell dataset. Both NLS runs detected increased MD in the lesion without overestimating FW or impacting FA. NLS was specific to both lesion types even when initialized with the single-shell hybrid method estimates (last column of Figures 5 and 6).

These results are quantitatively summarized in Figure 7, where the median and interquartile ranges for estimates inside the lesion mask are shown for the initial hybrid estimation, RGD single/multi-shell and NLS* fits (red, blue, green and cyan, respectively). Deviation of RGD quantities from the ground truth median (grey line) and interquartile ranges (grey shadow area) are smaller for the FW lesion (first column) than for the MD lesion (second column). NLS produced increased interquartile ranges (a consequence of its lower precision); however, it produces median values that closely match the expected ground truth values which confirming its higher accuracy.

5 Discussion

The FWE-DTI model was designed to quantify the fraction of free diffusing water molecules in biological tissue (18,19). Despite being based on a simplistic two-compartmental model, several studies showed FWE-DTI can be useful to eliminate confounding FW partial volume effects from standard DTI metrics, particularly in studies including subjects with varying degrees of tissue maturation or atrophy (20–22,30,31). The application of FWE-DTI to single-shell acquisitions remains, however, controversial. While some studies showed that plausible FW fractions can be obtained using RGD algorithms (19,27,34)], others have argued that such maps are unreliable since this model is degenerate for single-shell acquisitions (25,29). We aimed to address this controversy using representative in vivo data of a healthy human brain and synthetic signals with known ground truth parameters.

5.1 FWE-DTI provides plausible estimates

We confirm that plausible maps can be obtained from FWE-DTI applying RGD algorithms to single-shell datasets; FW fraction estimates obtained in this way present the expected hyperintensities in the cerebral ventricles and subarachnoid space and hypo-intensities in deep

WM (Figure 1). Moreover, RGD estimates fitted to a healthy subject single-shell dataset provides similar contrasts to well-posed standard FWE-DTI procedures fitted to multi-shell datasets. However, we stress that plausibility does not imply specificity (vide infra).

5.2 Initialization determines FWE-DTI plausibility

Single-shell FWE-DTI fitting procedures are based on two main steps: 1) fast parameter initialization; 2) refinement of initial estimates using RGD algorithms.

Considering the theory behind the initialization methods, a common feature is that all resort to prior information. Particularly, initialization based on T2-weighted information uses priors on the typical pure FW and tissue signals, initialization based on MD assumes a constant prior for MD_t , while the hybrid initialization is just a log interpolation between the former techniques. Resorting to these priors, a well-posed solution for an initial FW fraction (one unknown) can be obtained assuming that all other parameters are known - the water and tissue signals acquired with b-value=0 for the T2-weighted initialization (Eq. 3), or MD_t for the MD initialization (Eq. 5).

Refining the estimates when using the RGD algorithm attempted to use spatial information to improve the accuracy and precision of FWE-DTI estimates. Our numerical single-voxel simulations revealed that the initialization methods provide FW estimates somewhat sensitive to changes to the ground truth FW (Figure 2). Additionally, our synthetic multi-voxel phantom simulation showed that the FWE-DTI estimates refined by the RGD algorithm match the initial estimates when only single-shell data is provided (Figure 3). Based on these findings, we show that the plausibility of FWE-DTI initializations is the main determinant factor for the plausibility of FWE-DTI single-shell estimates.

5.3 Comparison across FWE-DTI initialization methods

Since initialization methods determine the plausibility of FWE-DTI contrasts for single-shell data, it is crucial to compare their robustness. Here, three initialization strategies were explored. We show that FWE-DTI initialization matches its ground truth only under certain conditions. Particularly, the f_w estimates for MD initialization matches the ground truth identity line only when the MD prior is identical to the ground truth values of $0.6 \mu m^2 ms^{-1}$ (first panel of Figure 2), while MD_t estimates for S_o initialization approach the ground truth identity line for synthetic signals generated with low FW (sixth panel of Figure 2).

In previous studies by Ismail and colleagues (31,34), these initialization methods were also compared, reporting final estimates closely matching the simulation ground truth values. However, the biases that can be induced when ground truth parameters deviate from the assumed priors had been barely considered. Indeed, our study shows that signals generated with MD_t larger than $0.6 \mu m^2 ms^{-1}$ can substantially inflate the FW fraction estimates for the MD initialization, leading to underestimated MD_t and overestimated FA values. On the other hand, although less dependent on the ground truth MD_t , the FW fraction estimates based on S_0 images present biases that depend on the ground truth FW content. Regarding the hybrid method, its estimates present an intermediate behavior, consistent with the fact that it interpolates between the MD and the S_0 based estimates, resulting in biases that depend on both MD_t and FW ground truth values. As this method presented lower biases than the MD based initialization for the single-voxel simulations and the lowest errors for the synthetic phantom (Figure 3), this technique was used for producing Figures 5, 6 and 7.

Although one might argue that initialization might be improved by adjusting the priors, constant priors cannot represent the expected biological variance of dwMRI signals. Indeed, even for healthy brain data, having a constant MD_t prior is inadequate for representing the variability of tissue's effective diffusivities across grey and WM regions presenting different microstructural properties. Additionally, selecting reference values for the FW and tissue signals (S_t , S_w) may be inadequate to capture the spatial variation of the T2-weighted images due to bias field inhomogeneities. Moreover, it is unlikely that such complex spatial patterns can be properly captured by a trivial combination of MD and S_0 initializations (as done by the hybrid method).

5.4 Assessment of FWE-DTI specificity

Given the expected heterogeneity of healthy tissue or pathological lesions, it is important to assess the robustness of FWE-DTI algorithms in simulations with ground truth parameters that represent the spatial variation of realistic dwMRI datasets. For this, the specificity of FWE-DTI was explored on synthetic datasets generated based on the parameter estimates obtained for a representative in vivo human brain dataset using the FWE-DTI gold standard technique (NLS fitting designed particularly for multi-shell dataset (25,29)).

Although FWE-DTI techniques can provide plausible estimates from single-shell data, plausibility is not equivalent to validity. While the priors imposed by the initialization techniques seem to provide sensitivity to the high FW fractions in brain cerebral ventricles and the subarachnoid space (Figure 1), the specificity of FWE-DTI can only be ensured if changes in FW

fraction can be distinguished from changes of the effective tissue diffusivity. To test for specificity, we assessed the performance of the different fitting algorithms on two different types of synthetic lesions. Our results show that when a lesion is generated for an increase of the FW fraction FWE-DTI hybrid initialization technique and consequently the RGD algorithm correctly predicts high FW volume fraction on the lesion area (Figure 5). However, when a lesion with increased MD_t was simulated, single-shell techniques barely detected a change in MD_t , and instead they erroneously predicted an increase in the FW fraction (Figure 6); Our results hence demonstrated that FWE-DTI specificity is not guaranteed for single-shell data.

5.5 Regularized descent algorithm in multi-shell data

While no advantage was observed for single-shell datasets, RGD seems to slightly improve the robustness of FW estimates. The measured FW fraction presented slightly increased precision on phantom simulations (Figure 4) and MD biases were suppressed on the MD lesion (Figure 5) when multi-shell acquisitions are considered. This result is consistent with RGD algorithms successfully converging to a more accurate solution only when multi-shell data is provided and when the FWE-DTI estimation becomes well-posed.

Interestingly, the refined FWE-DTI estimates never reached the accuracy of standard NLS FWE-DTI fitting procedures (Figures 5, 6 and 7). This might indicate that imposed spatial regularization might impede convergence to a global minimum. This contrasts with the performance of the NLS FWE-DTI algorithm which recovered the specificity of the estimates even when initialized with the single-shell hybrid initialization method. Although not shown here, single- and multi-shell RGD algorithm results were robust to changes in the learning rate and number of iterations. These observations are also in agreement with the findings of (34), where the authors noted that for data of two patients suffering from brain tumors the estimates obtained with and without the RGD algorithm were similar. In our work, we show that RGD algorithm, however, might present some benefits in terms of estimation precision.

5.6 Limitations and future work

The main limitation of our work is that FWE-DTI fitting routines were only tested on data and simulations reconstructed from a single healthy subject. Although not shown here, our analysis was repeated for other datasets available in DIPY showing consistent results. Since all our

implementations are available in an open-source project (dipy.org), the analysis can be easily reproduced for other open access data as the Human Connectome project (42) or the Biobank (43). Although we were able to demonstrate the limitations of the RGD algorithm using simplistic simulations, it will be of interest to reproduce the results on dwMRI data of real lesions or even on physical phantoms as proposed by Farrher and colleagues (44).

In this work, tissue's non-Gaussian diffusion effects due to the presence of multiple compartments or due to the interaction between diffusing water molecules and boundaries were not considered. As we wanted to separately assess the biases introduced by the priors of the FWE-DTI initialization methods and the spatial regularization of the gradient descent algorithm, we did not include data for b-values higher than $1 \text{ ms } \mu\text{m}^2$. However, previous studies showed that tissue non-Gaussian effects can also introduce biases on the FWE-DTI estimates even when obtained by the well-posed multi-shell NLS algorithm (25,45). In future studies, it will be of interest to assess if these biases can further compromise the specificity of FWE-DTI estimates on both single and multi-shell datasets.

The main findings of our work point to the need of moving from single-shell acquisitions to multi-shell protocols for proper fitting of the FWE-DTI model. In addition to the information provided by multi-shell acquisitions, this study may also motivate the exploration of techniques that incorporate other sources of information. For instance, FW and tissue components may be decoupled from the signal echo time dependence since these components are expected to have different T2 relaxation properties (46). The use of this type of information might be facilitated by the rise of acquisition approaches such as ZEBRA, enabling simultaneous measurement of different diffusion-weights and echo times (47) These approaches may not only aid in better characterizing tissue compartments but also enable to assess the true fractions of different compartments.

6 Conclusion

In this study, we address the controversies behind the use of regularized gradient descent algorithms to fit the FWE-DTI model on single- and multi-shell in vivo and synthetic datasets. Our results show that these algorithms can provide plausible FW fraction maps on both single- and multi-shell data, due to the priors introduced upon initialization. We show, however, that based solely on these priors, FWE-DTI estimates are not able to distinguish changes in FW content from

changes in MD_t for single-shell data acquisitions, and thus, we stress that results from single-shell FWE-DTI in previous and future studies should be interpreted with care.

7 Acknowledgements

We acknowledge the Portuguese Foundation for Science and Technology (FCT - IF/00364/2013, UID/EEA/50009/2019 and UIDB/50009/2020). We also want to thank Dr Valerij G. Kiselev (Freiburg University) for insightful discussions and suggestions, and Dr Valabregue Romain (CENIR, ICM, Paris) for supplying the open source dataset used in this study.

References

1. Le Bihan D, Iima M. Diffusion Magnetic Resonance Imaging: What Water Tells Us about Biological Tissues. *PLoS Biol* 2015;13:e1002203 doi: 10.1371/journal.pbio.1002203.
2. Basser PJ, Mattiello J, LeBihan D. MR diffusion tensor spectroscopy and imaging. *Biophys. J.* 1994;66:259–267 doi: 10.1016/S0006-3495(94)80775-1.
3. Jensen JH, Helpert JA, Ramani A, Lu H, Kaczynski K. Diffusional kurtosis imaging: the quantification of non-gaussian water diffusion by means of magnetic resonance imaging. *Magn Reson Med* 2005;53:1432–1440 doi: 10.1002/mrm.20508.
4. Neto Henriques R, Correia MM, Nunes RG, Ferreira HA. Exploring the 3D geometry of the diffusion kurtosis tensor--impact on the development of robust tractography procedures and novel biomarkers. *Neuroimage* 2015;111:85–99 doi: 10.1016/j.neuroimage.2015.02.004.
5. Cheung MM, Hui ES, Chan KC, Helpert JA, Qi L, Wu EX. Does diffusion kurtosis imaging lead to better neural tissue characterization? A rodent brain maturation study. *Neuroimage* 2009;45:386–392 doi: 10.1016/j.neuroimage.2008.12.018.
6. Nilsson M, van Westen D, Ståhlberg F, Sundgren PC, Lätt J. The role of tissue microstructure and water exchange in biophysical modelling of diffusion in white matter. *MAGMA* 2013;26:345–370 doi: 10.1007/s10334-013-0371-x.
7. Alexander AL, Hasan KM, Lazar M, Tsuruda JS, Parker DL. Analysis of partial volume effects in diffusion-tensor MRI. *Magn Reson Med* 2001;45:770–780 doi: 10.1002/mrm.1105.
8. Novikov DS, Kiselev VG, Jespersen SN. On modeling. *Magn Reson Med* 2018;79:3172–3193 doi: 10.1002/mrm.27101.
9. Assaf Y, Basser PJ. Composite hindered and restricted model of diffusion (CHARMED) MR imaging of the human brain. *Neuroimage* 2005;27:48–58 doi: 10.1016/j.neuroimage.2005.03.042.

10. Yablonskiy DA, Sukstanskii AL. Theoretical models of the diffusion weighted MR signal. *NMR Biomed* 2010;23:661–681 doi: 10.1002/nbm.1520.
11. Panagiotaki E, Schneider T, Siow B, Hall MG, Lythgoe MF, Alexander DC. Compartment models of the diffusion MR signal in brain white matter: a taxonomy and comparison. *Neuroimage* 2012;59:2241–2254 doi: 10.1016/j.neuroimage.2011.09.081.
12. Henriques RN, Jespersen SN, Shemesh N. Microscopic anisotropy misestimation in spherical-mean single diffusion encoding MRI. *Magn Reson Med* 2019;81:3245–3261 doi: 10.1002/mrm.27606.
13. Jespersen SN, Kroenke CD, Østergaard L, Ackerman JJH, Yablonskiy DA. Modeling dendrite density from magnetic resonance diffusion measurements. *Neuroimage* 2007;34:1473–1486 doi: 10.1016/j.neuroimage.2006.10.037.
14. Zhang H, Schneider T, Wheeler-Kingshott CA, Alexander DC. NODDI: practical in vivo neurite orientation dispersion and density imaging of the human brain. *Neuroimage* 2012;61:1000–1016 doi: 10.1016/j.neuroimage.2012.03.072.
15. Fieremans E, Jensen JH, Helpert JA. White matter characterization with diffusional kurtosis imaging. *Neuroimage* 2011;58:177–188 doi: 10.1016/j.neuroimage.2011.06.006.
16. Alexander DC, Hubbard PL, Hall MG, et al. Orientationally invariant indices of axon diameter and density from diffusion MRI. *Neuroimage* 2010;52:1374–1389 doi: 10.1016/j.neuroimage.2010.05.043.
17. Assaf Y, Blumenfeld-Katzir T, Yovel Y, Basser PJ. AxCaliber: a method for measuring axon diameter distribution from diffusion MRI. *Magn Reson Med* 2008;59:1347–1354 doi: 10.1002/mrm.21577.
18. Pierpaoli C, Jones DK. Removing CSF Contamination in Brain DT-MRIs by Using a Two-Compartment Tensor Model. *Proc. Intl. Soc. Mag. Reson. Med.* 2004:12–15.
19. Pasternak O, Sochen N, Gur Y, Intrator N, Assaf Y. Free water elimination and mapping from diffusion MRI. *Magn Reson Med* 2009;62:717–730 doi: 10.1002/mrm.22055.
20. O'Donnell LJ, Pasternak O. Does diffusion MRI tell us anything about the white matter? An overview of methods and pitfalls. *Schizophr. Res.* 2015;161:133–141 doi: 10.1016/j.schres.2014.09.007.
21. Papadakis NG, Martin KM, Mustafa MH, et al. Study of the effect of CSF suppression on white matter diffusion anisotropy mapping of healthy human brain. *Magnetic Resonance in Medicine* 2002;48:394–398 doi: 10.1002/mrm.10204.
22. Hoy AR, Ly M, Carlsson CM, et al. Microstructural white matter alterations in preclinical Alzheimer's disease detected using free water elimination diffusion tensor imaging. *PLoS ONE* 2017;12:e0173982 doi: 10.1371/journal.pone.0173982.
23. Planetta PJ, Ofori E, Pasternak O, et al. Free-water imaging in Parkinson's disease and atypical parkinsonism. *Brain* 2016;139:495–508 doi: 10.1093/brain/awv361.

24. Pasternak O, Koerte IK, Bouix S, et al. Hockey Concussion Education Project, Part 2. Microstructural white matter alterations in acutely concussed ice hockey players: a longitudinal free-water MRI study. *J. Neurosurg.* 2014;120:873–881 doi: 10.3171/2013.12.JNS132090.
25. Henriques RN, Rokem A, Garyfallidis E, St-Jean S, Peterson ET, Correia MM. [Re] Optimization of a free water elimination two-compartment model for diffusion tensor imaging. *Neuroscience*; 2017. doi: 10.1101/108795.
26. Liu G, van Gelderen P, Duyn J, Moonen CT. Single-shot diffusion MRI of human brain on a conventional clinical instrument. *Magn Reson Med* 1996;35:671–677 doi: 10.1002/mrm.1910350508.
27. Pasternak O, Maier-Hein K, Baumgartner C, Shenton ME, Rathi Y, Westin C-F. The Estimation of Free-Water Corrected Diffusion Tensors. In: Westin C-F, Vilanova A, Burgeth B, editors. *Visualization and Processing of Tensors and Higher Order Descriptors for Multi-Valued Data. Mathematics and Visualization.* Berlin, Heidelberg: Springer; 2014. pp. 249–270. doi: 10.1007/978-3-642-54301-2_11.
28. Scherrer B, Warfield S. Why multiple b-values are required for multi-tensor models. Evaluation with a constrained log-euclidean model. In: ; 2010. pp. 1389–1392. doi: 10.1109/ISBI.2010.5490257.
29. Hoy AR, Koay CG, Kecskemeti SR, Alexander AL. Optimization of a free water elimination two-compartment model for diffusion tensor imaging. *Neuroimage* 2014;103:323–333 doi: 10.1016/j.neuroimage.2014.09.053.
30. Bergmann Ø, Henriques R, Westin C-F, Pasternak O. Fast and accurate initialization of the free-water imaging model parameters from multi-shell diffusion MRI. *NMR Biomed* 2020;33:e4219 doi: 10.1002/nbm.4219.
31. Ismail AAO, Parker D, Hernandez-Fernandez M, et al. Characterizing Peritumoral Tissue Using Free Water Elimination in Clinical DTI. :10.
32. Garyfallidis E, Brett M, Amirbekian B, et al. Dipy, a library for the analysis of diffusion MRI data. *Front Neuroinform* 2014;8:8 doi: 10.3389/fninf.2014.00008.
33. Mills R. Self-diffusion in normal and heavy water in the range 1-45.deg. *J. Phys. Chem.* 1973;77:685–688 doi: 10.1021/j100624a025.
34. Ould Ismail AA, Parker D, Fernandez M, et al. Freewater Estimator using iNtErpolated iniTialization (FERNET): Toward Accurate Estimation of Free Water in Peritumoral Region Using Single-Shell Diffusion MRI Data.; 2019. doi: 10.1101/796615.
35. Gur Y, Pasternak O, Sochen N. Fast GL(n)-Invariant Framework for Tensors Regularization. *Int J Comput Vis* 2008;85:211 doi: 10.1007/s11263-008-0196-7.
36. Andersson JLR, Skare S, Ashburner J. How to correct susceptibility distortions in spin-echo echo-planar images: application to diffusion tensor imaging. *Neuroimage* 2003;20:870–888 doi: 10.1016/S1053-8119(03)00336-7.

37. Smith SM, Jenkinson M, Woolrich MW, et al. Advances in functional and structural MR image analysis and implementation as FSL. *Neuroimage* 2004;23 Suppl 1:S208-219 doi: 10.1016/j.neuroimage.2004.07.051.
38. Zhang Y, Brady M, Smith S. Segmentation of brain MR images through a hidden Markov random field model and the expectation-maximization algorithm. *IEEE Trans Med Imaging* 2001;20:45–57 doi: 10.1109/42.906424.
39. Abbas Z, Gras V, Möllenhoff K, Oros-Peusquens A-M, Shah NJ. Quantitative water content mapping at clinically relevant field strengths: A comparative study at 1.5T and 3T. *NeuroImage* 2015;106:404–413 doi: 10.1016/j.neuroimage.2014.11.017.
40. Wansapura JP, Holland SK, Dunn RS, Ball WS. NMR relaxation times in the human brain at 3.0 tesla. *Journal of Magnetic Resonance Imaging* 1999;9:531–538 doi: 10.1002/(SICI)1522-2586(199904)9:4<531::AID-JMRI4>3.0.CO;2-L.
41. Piechnik SK, Evans J, Bary LH, Wise RG, Jezzard P. Functional changes in CSF volume estimated using measurement of water T2 relaxation. *Magnetic Resonance in Medicine* 2009;61:579–586 doi: 10.1002/mrm.21897.
42. Van Essen DC, Smith SM, Barch DM, et al. The WU-Minn Human Connectome Project: an overview. *Neuroimage* 2013;80:62–79 doi: 10.1016/j.neuroimage.2013.05.041.
43. Miller KL, Alfaro-Almagro F, Bangerter NK, et al. Multimodal population brain imaging in the UK Biobank prospective epidemiological study. *Nat. Neurosci.* 2016;19:1523–1536 doi: 10.1038/nn.4393.
44. Farrher E, Grinberg F, Kuo L-W, et al. Dedicated diffusion phantoms for the investigation of free water elimination and mapping: insights into the influence of T2 relaxation properties. *NMR in Biomedicine* 2020;33:e4210 doi: 10.1002/nbm.4210.
45. Neto Henriques R. *Advanced Methods for Diffusion MRI Data Analysis and their Application to the Healthy Ageing Brain [Thesis]*. University of Cambridge; 2018. doi: 10.17863/CAM.29356.
46. Veraart J, Novikov DS, Fieremans E. TE dependent Diffusion Imaging (TEdDI) distinguishes between compartmental T2 relaxation times. *NeuroImage* 2018;182:360–369 doi: 10.1016/j.neuroimage.2017.09.030.
47. Hutter J, Sator PJ, Christiaens D, et al. Integrated and efficient diffusion-relaxometry using ZEBRA. *Scientific Reports* 2018;8:15138 doi: 10.1038/s41598-018-33463-2.

Figures

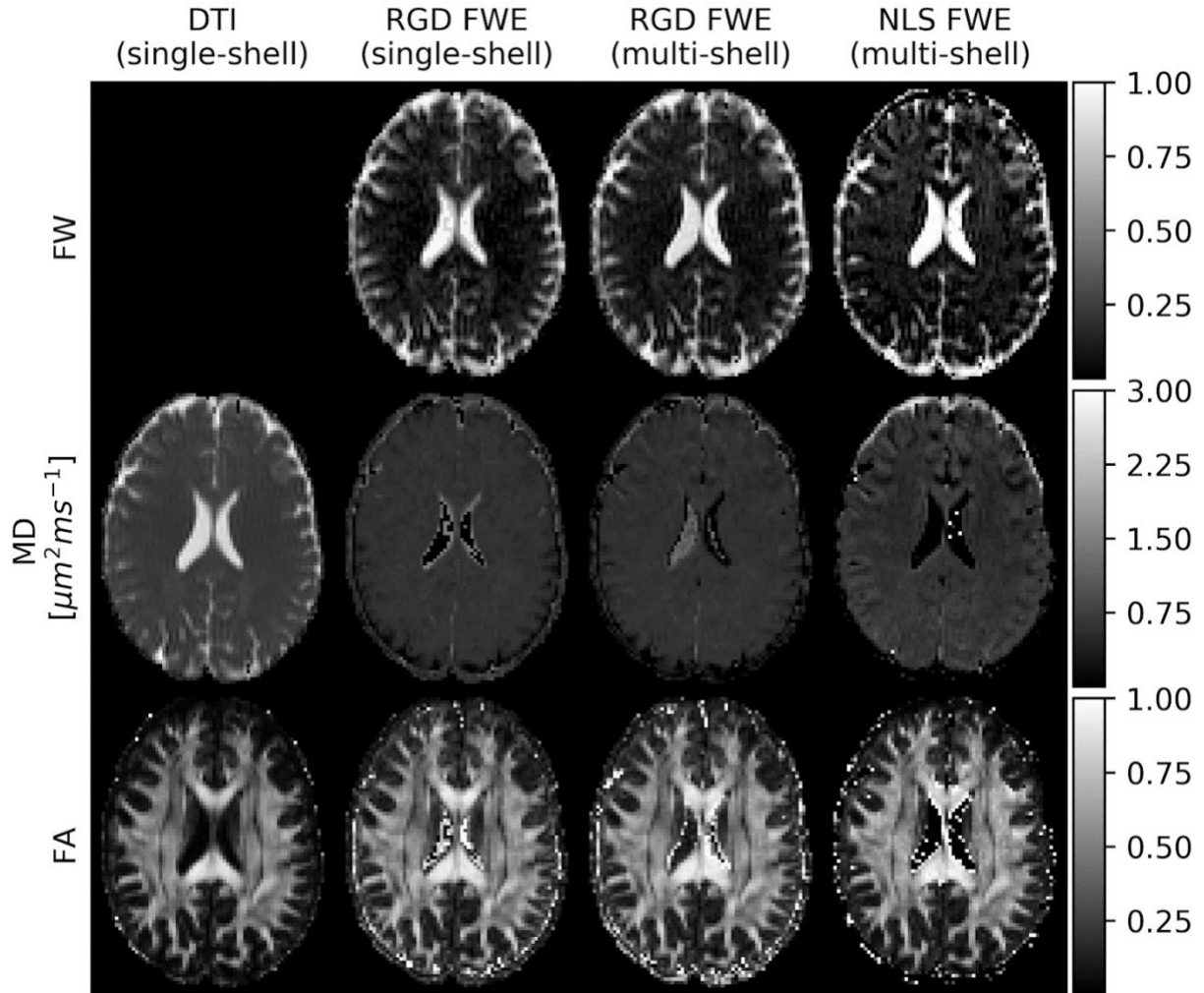


Figure 1: Scalar maps estimated from data acquired from a healthy volunteer (free water fraction [f_w], mean diffusivity [MD], and fractional anisotropy [FA] shown in the first, second and third rows, respectively), using standard DTI (first column), regularized gradient descent (RGD), FWE-DTI for single- and multi-shell data (second and third columns) and NLS FWE-DTI (fourth column). For the single-shell maps, data acquired with b-values of $1\text{ ms } \mu\text{m}^{-2}$ was used; for the multi-shell maps, all b-values up to $1\text{ ms } \mu\text{m}^{-2}$ were used.

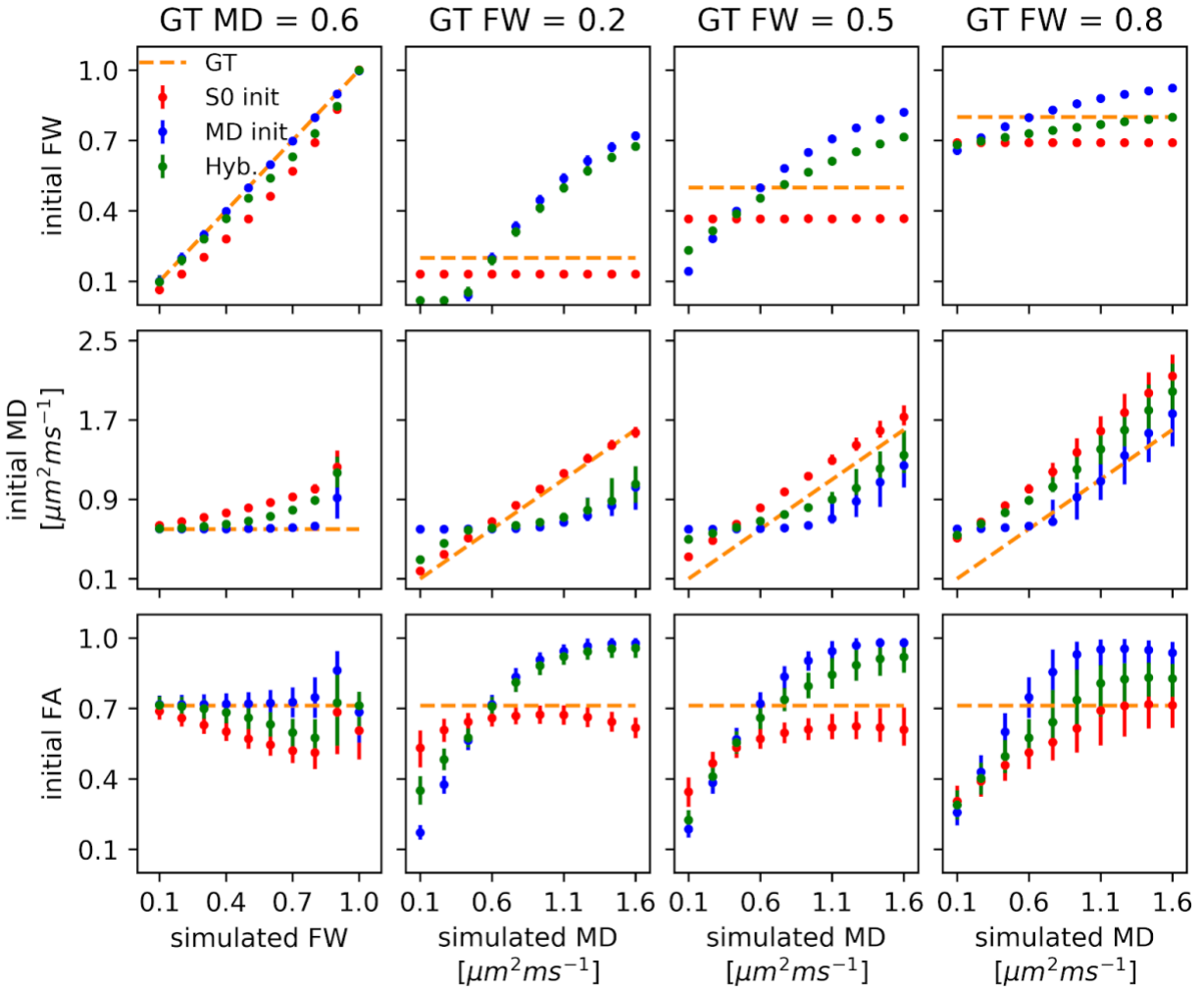


Figure 2: Median and interquartile ranges of the initial f_w , MD_t and FA (top, middle and bottom rows, respectively) applied to single-voxel signals over 10,000 repeats (100 D_t directions \times 100 noise instances). These values are plotted as a function of f_w ground truth values (from 0 to 1) on the left column (for a fixed ground truth $MD_t=0.6 \mu m^2 ms^{-1}$) and plotted as a function of MD_t ground truth values (from 0.1 to 1.6 $\mu m^2 ms^{-1}$) on the second to fourth columns (for fixed f_w ground truth values of 0.2, 0.5 and 0.8, respectively). On each panel, ground truth values are represented by the orange lines, S_0 initialization estimates by the red markers, MD_t initialization estimates by the blue markers, while hybrid initialization corresponds to the green markers.

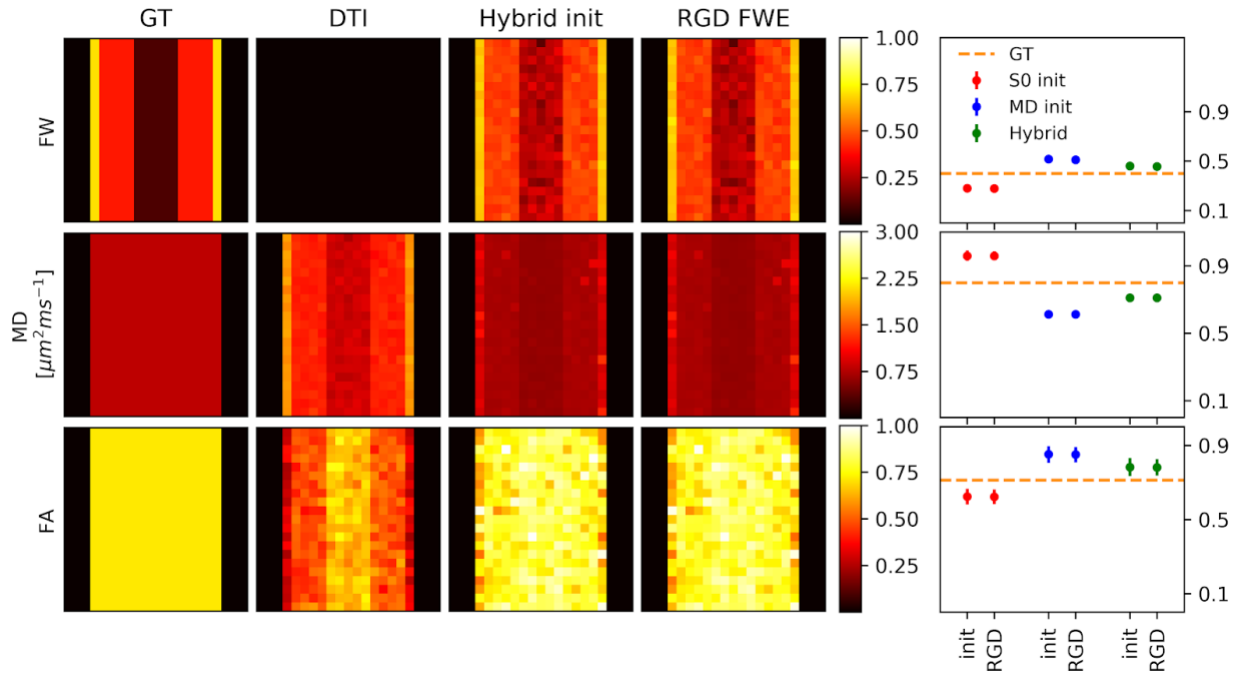


Figure 3: Results for the single-shell dataset of the multi-voxel phantom. On the left side of the figure, the f_w , FA and MD parametric map estimates are shown for the ground truth values (first column), standard DTI (second column), FWE-DTI hybrid initialization (third column), and FWE-DTI regularized gradient descent (RGD) algorithm initialized using the hybrid method (fourth column). On the right side, the corresponding distributions are plotted for the estimates before ('init') and after ('est') applying the RGD algorithm and for the three initialization methods - S_0 , MD_t and hybrid initializations (red, blue and green, respectively) compared to the GT (orange). To enable an easier interpretation, the median and interquartile rates were computed inside the region with intermediate GT f_w value of 0.4 (similar conclusions could be drawn for the other GT f_w values - results not shown).

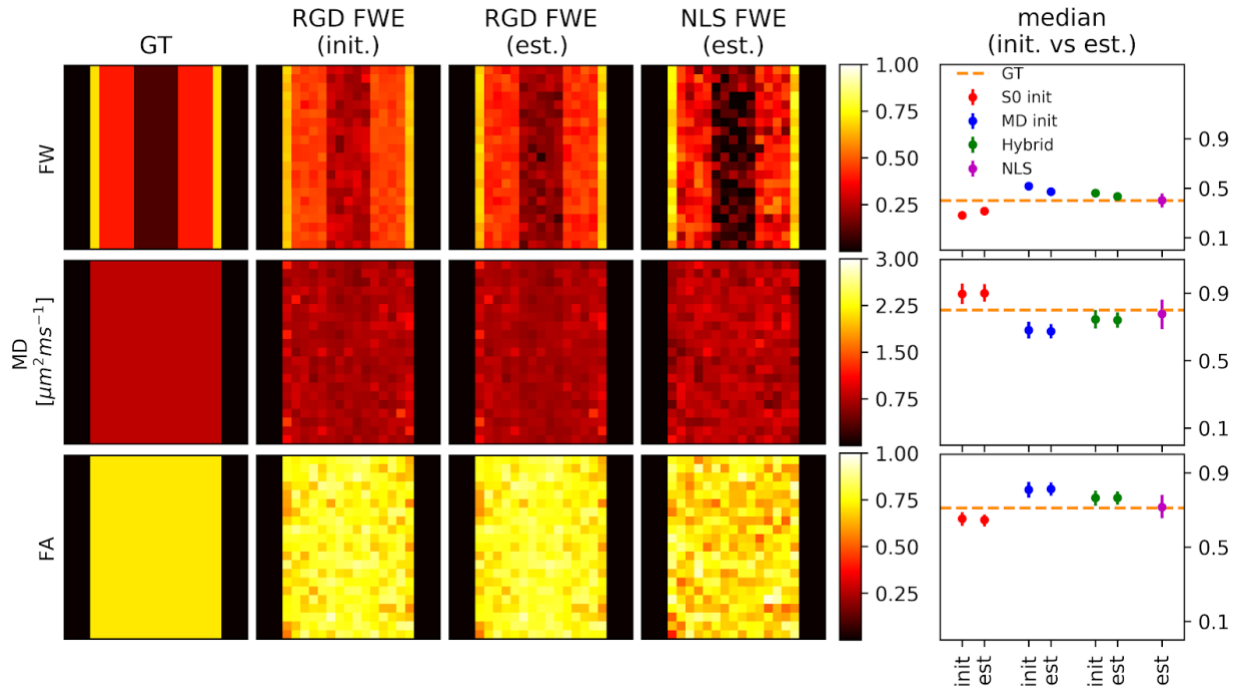


Figure 4: Results for the multi-shell dataset of the multi-voxel phantom. On the left side of the figure, the parametric maps of fw, FA and MD estimates are shown for the ground truth values (first column), FWE-DTI hybrid initialization (second column), FWE-DTI regularized descent algorithm (RGD) initialized using the hybrid method (third column), and the NLS FWE-DTI algorithm (fourth column). On the right side of the figure, the corresponding distributions are plotted for the estimates before ('init') and after ('est') applying the RGD algorithm and for the three initialization methods - S0, MDt and hybrid initialization (red, blue and green, respectively) compared to the GT (orange). To enable an easier interpretation, the median and interquartile rates were computed inside the region with intermediate GT fw value of 0.4 (similar conclusions could be drawn for the other GT fw values - results not shown).

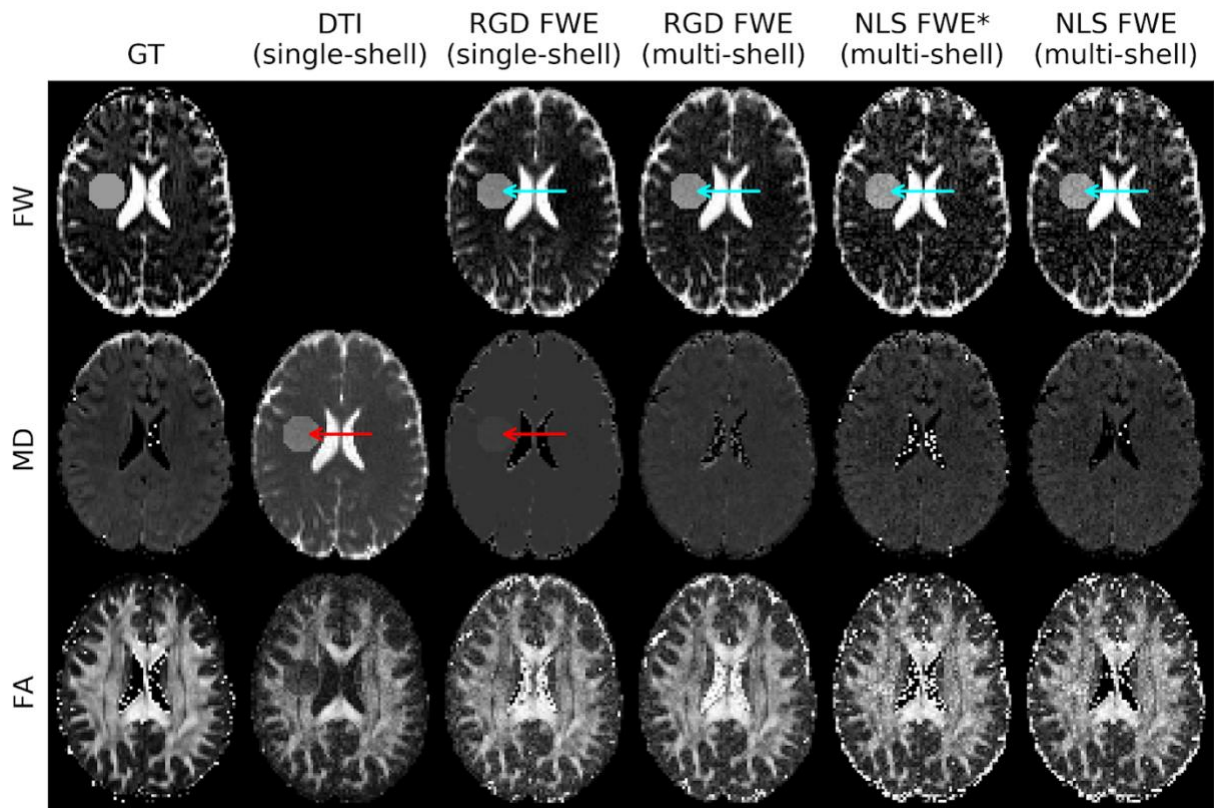


Figure 5: Scalar maps estimated from in vivo data after introducing a simulated FW lesion. The ground truth (GT) is represented on the first column, while the remaining columns show the estimates obtained using standard DTI (second column), RGD FWE-DTI for single- and multi-shell data (third and fourth columns) and NLS FWE-DTI (fifth column). The NLS FWE-DTI* (sixth column) shares the same initialization method used in the RGD routine (hybrid approach). The single-shell data was simulated along 32 directions with $b=1 \text{ ms } \mu\text{m}^{-2}$ (in addition to six $b\text{-value}=0$ images); the multi-shell data was simulated with b -values of $0.5 \text{ ms } \mu\text{m}^{-2}$ and $1 \text{ ms } \mu\text{m}^{-2}$ (32 directions each, in addition to six $b\text{-value}=0$ images).

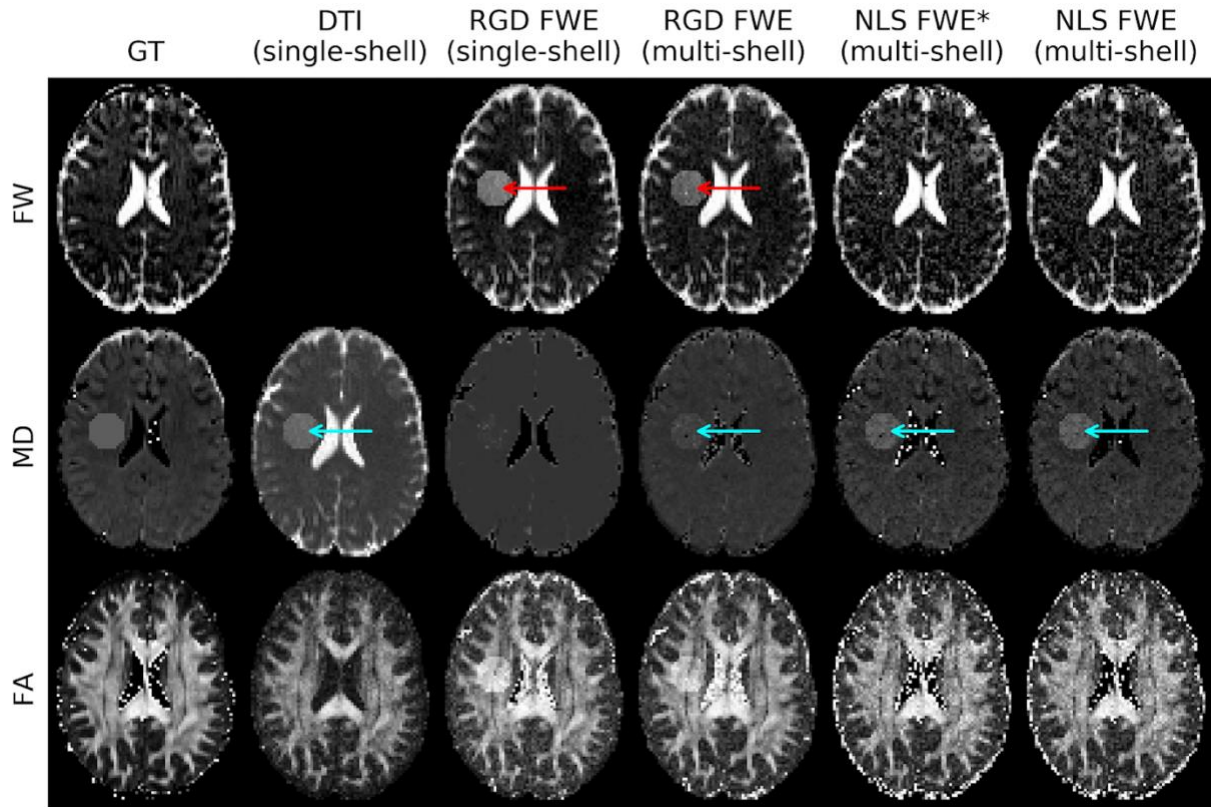


Figure 6: Scalar maps estimated from in vivo data after introducing a simulated MD lesion. The ground truth (GT) is represented on the first column, while the remaining columns show the estimates obtained using standard DTI (second column), RGD FWE-DTI for single- and multi-shell data (third and fourth columns) and NLS FWE-DTI (fifth column). The NLS FWE-DTI* (sixth column) shares the same initialization method used in the RGD routine (hybrid approach). The single-shell data was simulated along 32 directions with $b=1 \text{ ms } \mu\text{m}^{-2}$ (in addition to six $b\text{-value}=0$ images); the multi-shell data was simulated with $b\text{-values}$ of $0.5 \text{ ms } \mu\text{m}^{-2}$ and $1 \text{ ms } \mu\text{m}^{-2}$ (32 directions each, in addition to six $b\text{-value}=0$ images).

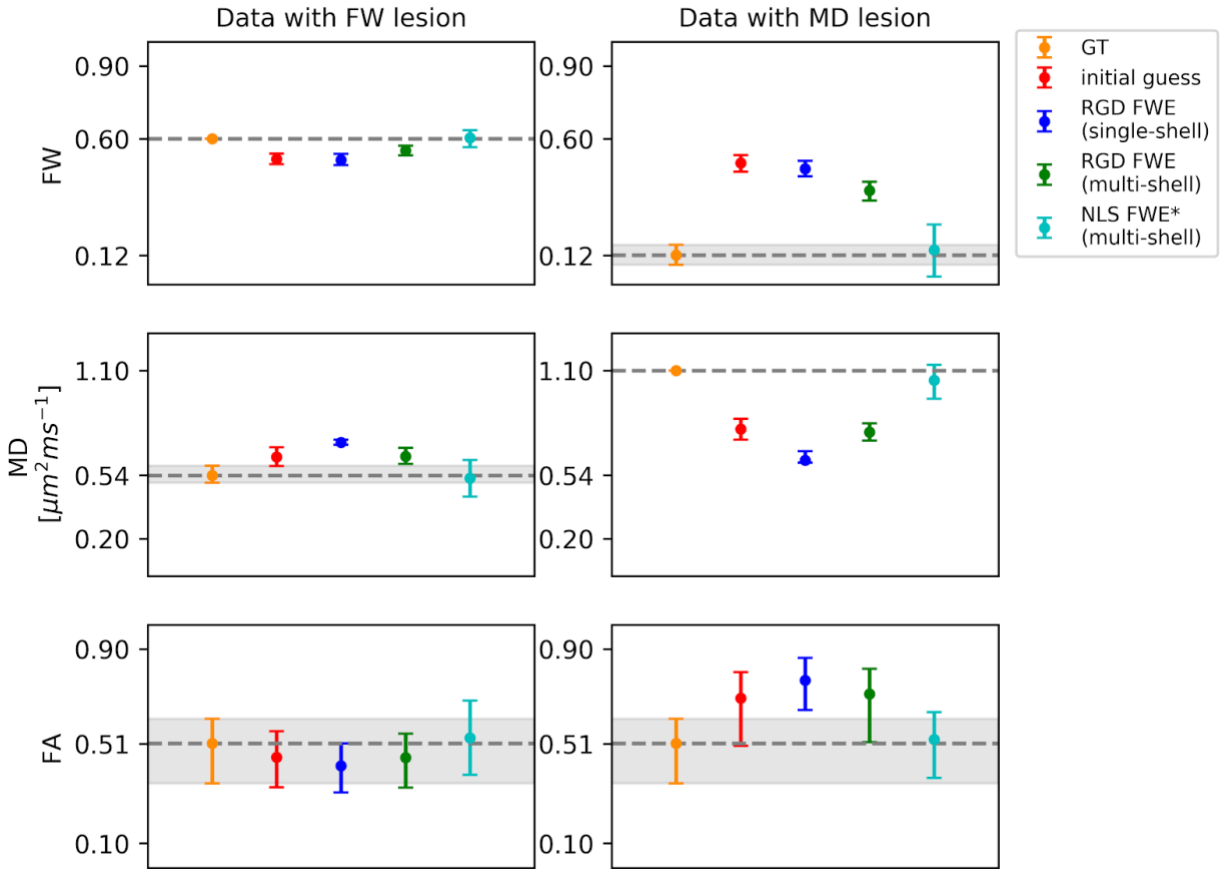


Figure 7: Distribution of the f_w , MD , and FA estimates (first, second and third rows) extracted from the FW lesion (left panels) and MD lesion (right panels). The markers correspond to the median values while the bars represent the interquartile range computed inside the lesion. On each panel estimates from the initial hybrid method, RGD single- and multi-shell methods and modified NLS fitting routines are plotted in red, blue, green, and cyan respectively and compared to the ground truth (GT) (orange). To facilitate comparisons, a dashed grey line indicates the median GT value, with the shaded areas representing its interquartile range.